

Orbital mixing and nesting in the bilayer manganites $\text{La}_{2-2x}\text{Sr}_{1+2x}\text{Mn}_2\text{O}_7$

R. Saniz,^{1,*} M. R. Norman,² and A. J. Freeman¹

¹*Department of Physics and Astronomy, Northwestern University, Evanston, Illinois 60208*

²*Materials Science Division, Argonne National Laboratory, Argonne, Illinois 60439*

(Dated: February 2, 2022)

A first principles study of $\text{La}_{2-2x}\text{Sr}_{1+2x}\text{Mn}_2\text{O}_7$ compounds for doping levels $0.3 \leq x \leq 0.5$ shows that the low energy electronic structure of the majority spin carriers is determined by strong momentum dependent interactions between the Mn e_g $d_{x^2-y^2}$ and $d_{3z^2-r^2}$ orbitals, which in addition to an x dependent Jahn-Teller distortion, differ in the ferromagnetic and antiferromagnetic phases. The Fermi surface exhibits nesting behavior that is reflected by peaks in the static susceptibility, whose positions as a function of momentum have a non-trivial dependence on x .

PACS numbers: 71.18.+y, 71.20.-b, 75.40.Gb, 75.47.Lx

One of the most studied series of compounds over the past decade, having being scrutinized using a wide range of experimental methods [1], is that of the bilayer manganites $\text{La}_{2-2x}\text{Sr}_{1+2x}\text{Mn}_2\text{O}_7$, with new findings of their basic properties continuing to emerge [2, 3]. Their interest is due to several reasons. It is well known that they exhibit a colossal magnetoresistive effect around critical temperatures of 100-200 K, depending on the doping level x [1]. A proper understanding of this phenomenon should point the way to tailoring materials with higher critical temperatures, which could potentially lead to magnetic devices that would outperform present ones based on the giant magnetoresistive effect. On the fundamental side, it is thought that the properties of these materials are due to an interplay of structural, orbital, and magnetic degrees of freedom, a trait shared by several strongly correlated materials, including the superconducting cuprates [4]. In the case of the manganites, there is no consensus as yet on exactly how these different degrees of freedom lead to the observed properties. Elucidating this will no doubt lead to an advance in our understanding of related phenomena in the broader context of higher complexity condensed matter systems.

One of the reasons for the current state of affairs is that the ground state properties of the bilayer manganites are not completely understood, even at low temperatures. From the theoretical standpoint, there are few published reports of *ab initio* calculations of the electronic structure of these compounds [5]. While these studies have provided an important framework for the analysis of experiments, several observations remain to be addressed. For instance, it is generally recognized that it is the character of the occupied Mn e_g states that determines the key properties of these systems, such as the conductivity and the nature of the magnetic order. Thus, important efforts have been made to understand the orbital polarization of these states [6, 7, 8, 9], but the problem has only been partially addressed from an *ab initio* perspective [10]. In this work, we present a first principles study of the conducting states of the bilayer manganites for hole doping levels $0.3 \leq x \leq 0.5$. We show that the $d_{x^2-y^2}$ and

$d_{3z^2-r^2}$ orbitals strongly mix, with the mixing depending not only on x , but also on the direction in \mathbf{k} -space. This has a pronounced impact on the Fermi surface topology and nesting, long suggested to play an important role in these materials [11, 12, 13]. This is illustrated by calculating the static susceptibility $\chi(\mathbf{q})$, which indeed shows peaks due to nesting. The implications of our work in relation to recent experiments are discussed.

We employ the highly precise all-electron full-potential linearized augmented plane wave (FLAPW) implementation of density functional theory [14], with the generalized gradient approximation (GGA) [15, 16] for the exchange-correlation potential. For $x < 0.5$, we use the “charged cell” approximation, i.e., increasing the valence electron number by the required amount and adding a uniform positive charge for neutrality [17]. The calculations were carried out for the observed magnetic phases: ferromagnetic (FM) for $x \leq 0.4$ and antiferromagnetic (AF) for $x \geq 0.45$. In our calculations, the AF phase is given by ferromagnetic MnO_2 planes that are coupled antiferromagnetically within a bilayer as well as between adjacent bilayers. Though in experiment the latter coupling is ferromagnetic in the A-type AF order, it is known to be very weak [1], and so should not influence our results [16]. As for technical aspects of the calculations, convergence was assured with respect to muffin-tin radii, \mathbf{k} -point mesh [1164 points in the irreducible wedge of the Brillouin zone], and energy cut-offs. The structural parameters for each x ($I4/mmm$) are from Ref. 18 at 10 K. We assume La is in the 2b and Sr in the 4e sites [19].

As indicated above, key to the understanding of the bilayer manganites is the relative role of the e_g states ($d_{x^2-y^2}$ and $d_{3z^2-r^2}$) [1]. To illustrate these states, we refer to the band structure plots in Fig. 1 (simple tetragonal symmetry notation is used). Two cases are shown, namely $x = 0.5$ (AF) and $x = 0.4$ (FM). The states with more than 50% Mn d character are highlighted with dots. In the AF case, there is Kramers degeneracy, so the two spin states are interchanged for the second Mn atom type (there is only one Mn atom type in the FM case). In the following, we focus on the e_g states.

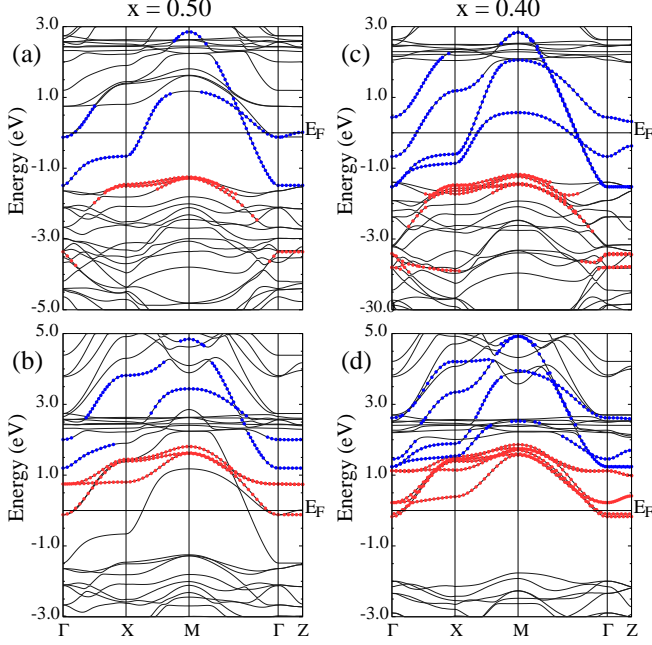


FIG. 1: (color online) Band structure of $\text{LaSr}_2\text{Mn}_2\text{O}_7$ ($x = 0.5$, AF phase) for \uparrow [\downarrow] spin in panel (a) [(b)], and of $\text{La}_{1.2}\text{Sr}_{1.8}\text{Mn}_2\text{O}_7$ ($x = 0.4$, FM phase) for \uparrow [\downarrow] spin in panel (c) [(d)]. The gray (red) and black (blue) dots highlight states of dominant Mn t_{2g} and e_g character, respectively.

The basic electronic structure near the Fermi energy (E_F) can be understood as arising from the two Mn $d_{x^2-y^2}$ and two Mn $d_{3z^2-r^2}$ orbitals per bilayer. Ignoring orbital mixing and hybridization with other states, in the FM case the energy of each orbital would be of the form $\epsilon_i \pm X \pm \Delta$, where ϵ_i is the unpolarized atomic orbital energy ($i = 1, 2$), $2X$ the exchange splitting, and 2Δ the bilayer splitting, resulting in eight states altogether. In contrast, in the AF case the energy of each orbital would be of the form $\epsilon_i \pm \sqrt{X^2 + \Delta^2}$, resulting in four Kramers degenerate states. Since $X \gg \Delta$, the bilayer splitting is essentially quenched in the AF case. Consequently, as we show below, there is only one barrel centered at M in the AF case, as opposed to two in the FM case. Moreover, for the AF case, unlike the FM one, we do not expect a strong intensity modulation of the photoemission signal as a function of photon energy due to bilayer splitting.

In the actual calculations the two e_g orbitals are mixed. This is directly reflected in the Fermi surface topology. In Fig. 2(a), we show the Fermi surface for $x = 0.5$ (AF), and in Fig. 2(b) for $x = 0.4$ (FM, majority spin). In the AF case, there is a hole-like barrel centered at M of mainly $d_{x^2-y^2}$ symmetry (labeled 1), a prolate electron-like sheet around Γ of $d_{3z^2-r^2}$ symmetry (labeled 2), and a (minority spin) cylindrical sheet centered at Γ of d_{xy} symmetry (labeled 3). In the FM phase, there is a hole-like barrel of dominant $d_{x^2-y^2}$ symmetry centered at M (labeled 1), and two barrels of mixed $d_{x^2-y^2}$ and $d_{3z^2-r^2}$

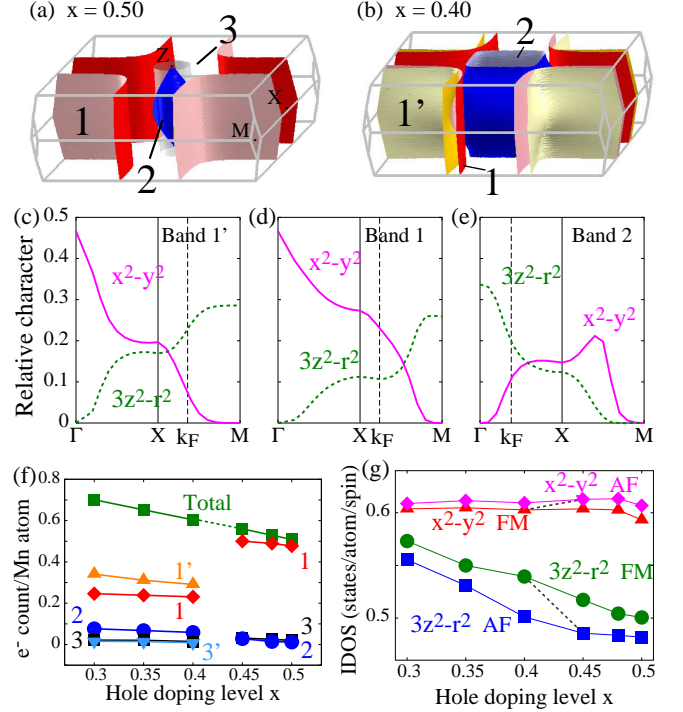


FIG. 2: (color online) Fermi surface for (a) $x = 0.5$ (AF) and (b) $x = 0.4$ (FM). (c), (d), and (e): Orbital character of the states along the Γ -X-M line for the e_g bands crossing E_F for $x = 0.4$. (f) Luttinger count of the different Fermi surface sheets, and (g) integrated density of states (IDOS) for $d_{x^2-y^2}$ and $d_{3z^2-r^2}$ as a function of doping, imposing either AF or FM order. Note the crossover in orbital population due to the change in magnetic order (dotted lines).

symmetry: one hole-like, centered at M (labeled 1'), and the other electron-like, centered at Γ (labeled 2) [20].

The mixing is shown by an analysis of the character of the states for bands crossing E_F . For example, in Fig. 2(c) we show the character of the lower e_g band (1') for $x = 0.4$ (FM) and \mathbf{k} points along the Γ -X-M directions. It starts with $d_{x^2-y^2}$ character at Γ , but when reaching X, the mixing with $d_{3z^2-r^2}$ is about 50%. At k_F , roughly halfway between X and M, the character becomes dominantly $d_{3z^2-r^2}$. The middle band (1), in contrast [Fig. 2(d)], has a fairly dominant $d_{x^2-y^2}$ character up to k_F , at about a quarter of the X-M distance. Band 2, in turn [Fig. 2(e)], starts out at Γ as $d_{3z^2-r^2}$ but is strongly mixed at k_F . Thus, it is inaccurate to characterize the barrels around the M point as ' $x^2 - y^2$ ', and the electron pocket around Γ as ' $3z^2 - r^2$ '. Our results for the other doping levels in the FM phase show that the orbital mixing increases with decreasing x , and that the bilayer splitting becomes stronger. A similar analysis shows that in the AF case, the lower e_g band (1) is of dominant $d_{x^2-y^2}$ character, but with strong mixing at k_F along X-M. The upper band (2) is $d_{3z^2-r^2}$ like.

Of further relevance to experiment is the occupation

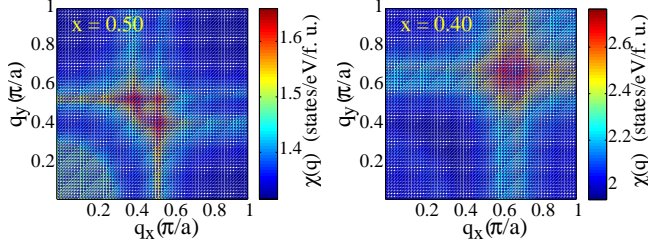


FIG. 3: (color online) The static susceptibility, $\chi(\mathbf{q})$, for $\mathbf{q} = (q_x, q_y, 2\pi/c)$, for $x = 0.5$ (AF) and $x = 0.4$ (FM).

level of the bands crossing E_F . Thus, we calculated the carrier number by integrating the volume enclosed by the different Fermi surfaces (the Luttinger count). We used a fine mesh of 32340 \mathbf{k} -points in the irreducible wedge, and the results as a function of x are shown in Fig. 2(f). In the AF phase, sheet 1 is obviously dominant. In the FM phase, the Kramers degeneracy is lifted, giving rise to sheets 1 and 1'. The increased orbital mixing lowers the energy, particularly in the case of states 1', allowing the charge to increase as x decreases. In the FM phase there is only one sheet 2 because the antibonding counterpart is empty (due to the large bilayer splitting of $3z^2 - r^2$ in the FM phase). Thus, the electron pocket around Γ roughly doubles in size compared to the AF phase. Note that for $0.4 < x \lesssim 0.45$ the actual phase is a canted antiferromagnet [18], so the bilayer splitting is probably reduced gradually with x . But clearly, AF coupling acts to quench the bilayer splitting, with dramatic effects, particularly for the $d_{3z^2-r^2}$ states. This is in line with very recent photoemission data that indicate a collapse of bilayer splitting near $x=0.4$ [21, 22].

In Fig. 2(g) we plot the e_g orbital occupation counts (estimated by integrating the muffin-tin projected density of states) as a function of x , imposing either a FM or AF phase. The $d_{x^2-y^2}$ orbital population is not strongly affected across the FM-AF transition, but the $d_{3z^2-r^2}$ orbital population significantly increases in the FM phase. This agrees with conclusions from magnetic Compton scattering measurements [6]. Further, our results show a striking cooperative effect between Jahn-Teller distortion and magnetic order. Indeed, the evolution of the occupations with x in a given magnetic phase reflects the change of the apical Mn-O bond lengths [18]. But the crossover due to the change in magnetic order (dotted line) is largely due to the change in bilayer splitting.

The above results also indicate that the possible nesting instabilities suggested to play an important role in these materials [11, 13] have a non-trivial dependence on x . To see this, we calculated the generalized charge susceptibility (constant matrix element approximation)

$$\chi(\mathbf{q}, \omega \rightarrow 0) = \frac{1}{N} \sum_{n, \mathbf{m}} \sum_{\mathbf{k}, \sigma} \frac{f_{n\mathbf{k}\sigma}(1 - f_{m\mathbf{k}+\mathbf{q}\sigma})}{\epsilon_{m\mathbf{k}+\mathbf{q}\sigma} - \epsilon_{n\mathbf{k}\sigma} - \omega}. \quad (1)$$

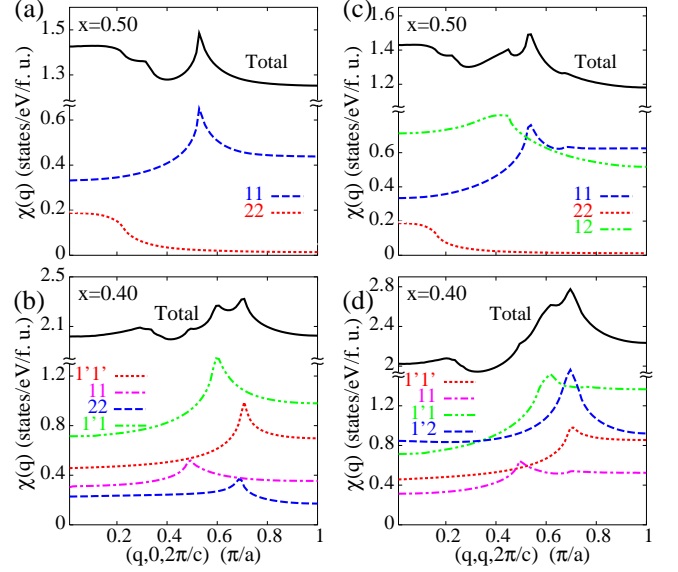


FIG. 4: (color online) Static susceptibility $\chi(\mathbf{q})$ for \mathbf{q} along two symmetry directions for $x = 0.5$ (AF) and $x = 0.4$ (FM). The labels indicate which band transitions are responsible for the structure in χ . Labeling corresponds to that in Fig. 2. Note the break in the vertical axis.

For this calculation, we again used 32340 \mathbf{k} -points in the irreducible wedge and the tetrahedron method with linear interpolation [23]. In Fig. 3, we show $\chi(\mathbf{q})$ for \mathbf{q} of the form $(q_x, q_y, 2\pi/c)$. This is of interest because diffuse x-ray scattering data have shown peaks for $q_z = 2\pi/c$ in the $x = 0.4$ compound [24]. Both the AF and FM cases show clear peaks and kinks correlating closely with the topology of the Fermi surface. The calculations were done taking into account only the bands crossing E_F . We verified that including more bands does not affect significantly the momentum structure of the response. Also, the e_g to t_{2g} transitions were ignored to crudely simulate the neglected matrix elements effects. We note that the t_{2g} transitions mostly contribute to a diffuse response centered at Γ , so we focus on the e_g transitions only.

Figure 4 takes a closer look for \mathbf{q} along two directions. For $\mathbf{q} = (q, 0, 2\pi/c)$, Fig. 4(a) (AF) shows a strong peak at $q = 0.53$ (11 transition). The interband transition (12) has little structure (not shown). Figure 4(b) (FM) shows two main peaks, for $q = 0.62$ (1'1' transition), and 0.71 (1'1' and 22 transitions). The peak arising from 11 transitions is relatively weaker in the FM case. It is significant that the 1'1' peak at this doping level matches the bond centered peak reported at $q = 0.6$ in Ref. 24. For $\mathbf{q} = (q, q, 2\pi/c)$, Fig. 4(c) (AF) shows the same (11) peak as Fig. 4(a), and a less well defined maximum at $q = 0.42$ (12 transition). This maximum is equally ill-defined at other doping levels. Fig. 4(d) (FM) shows a clearly dominant peak at $q = 0.7$ arising from mainly 1'1' and 1'2 transitions. We point out that the two kinks for smaller q (1'1' and 11) are weaker at lower doping levels

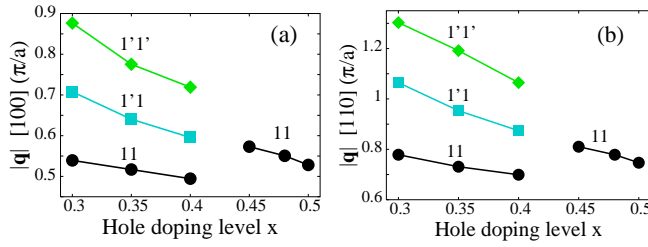


FIG. 5: (color online) Nesting vector lengths (extracted from the peaks in χ) as a function of doping level x for \mathbf{q} along (a) the [100] and (b) [110] directions.

because of strong broadening of these features.

Finally, in Fig. 5 we consider the dependence on x of the lengths of the magnitude of the nesting vectors along the [100] and [110] directions, inferred previously from photoemission [11, 12]. We extracted these from the peaks in χ corresponding to those in Fig. 4. Again, we remark that we do not have results for the actual canted phase for $0.45 \lesssim x < 0.5$. Note that the 11 vector for $x = 0.4$ in the [110] direction matches that of the so-called CE-ordering wave vector [11]. We particularly point to the jump of the 11 nesting vector when the magnetic phase changes. Clearly, this is due to the ‘turning on’ of the bilayer splitting in the FM phase. Again, this illustrates dramatically the correlation between $d_{3z^2-r^2}$ and $d_{x^2-y^2}$ orbital mixing, bilayer splitting, and FM order. Further, this jump may explain the non-monotonic x -dependence of the nesting vector recently inferred from photoemission and diffuse scattering measurements [25]. The charge ordering peaks observed in the latter are either along the bond direction, the diagonal, or both, depending on the doping level. Typically, the diagonal response is largest, since although the nesting is not as good for such vectors, twice as many Fermi surface faces are brought into coincidence as compared to the bond oriented case [26]. We also note that in the FM phase, for transitions involving 1', the peak structure for $q_z = 0$ along the bond direction is less distinct than for $q_z = 2\pi/c$. This is because of the ‘tilting’ of the 1' surface (a consequence of its strong $d_{3z^2-r^2}$ admixture), which alternates in direction between $q_z = 0$ and $2\pi/c$ due to the c -axis dispersion. For the same reason, the diagonal peaks involving 1' are stronger for $q_z = 0$. This may explain why the diffuse scattering peaks occur for $q_z = 2\pi/c$ for the bond directions and $q_z = 0$ for the diagonal directions [24, 25].

In summary, we find that mixing of the Mn $d_{x^2-y^2}$ and $d_{3z^2-r^2}$ orbitals and bilayer splitting play a fundamental role in the electronic structure of the bilayer manganites, particularly in the FM phase, and correlate closely with the transition from FM to AF order with doping. These two effects result in different Fermi surface topologies for the two phases. As a result, the static susceptibility, and

the e_g orbital polarization, are predicted to have a non-monotonic dependence on doping due to the change from FM to AF order as the hole doping level increases.

We acknowledge the support of the US DOE, Office of Science, under Grant No. DE-FG02-88ER45372 and Contract No. DE-AC02-06CH11357, and a computer time grant at the NERSC. We thank B. Barbiellini, L.-H. Ye, J.-H. Song, J. F. Mitchell, R. Osborn, S. Rosenkranz, U. Chatterjee and J. C. Campuzano for useful discussions.

* Present address: Departement Fysica, Universiteit Antwerpen, Groenenborgerlaan 171, B-2020 Antwerpen, Belgium.

- [1] T. Kimura and Y. Tokura, *Annu. Rev. Mater. Sci.* **30**, 451 (2000).
- [2] N. Mannella *et al.*, *Phys. Rev. B* **76**, 233102 (2007).
- [3] S. de Jong *et al.*, *Phys. Rev. B* **76**, 235117 (2007).
- [4] E. Dagotto, *Science* **309**, 257 (2005).
- [5] X. Y. Huang *et al.*, *Phys. Rev. B* **62**, 13318 (2000).
- [6] A. Koizumi *et al.*, *Phys. Rev. Lett.* **86**, 5589 (2001).
- [7] Y. Li *et al.*, *Phys. Rev. Lett.* **93**, 207206 (2004).
- [8] B. Barbiellini *et al.*, *J. Phys. Chem. Solids* **66**, 2197 (2005).
- [9] A. Koizumi *et al.*, *Phys. Rev. B* **74**, 012408 (2006).
- [10] P. E. Mijnarends *et al.*, *Phys. Rev. B* **75**, 014428 (2007).
- [11] Y.-D. Chuang *et al.*, *Science* **292**, 1509 (2001).
- [12] Z. Sun *et al.*, *Phys. Rev. Lett.* **97**, 056401 (2006).
- [13] M. W. Kim *et al.*, *Phys. Rev. Lett.* **98**, 187201 (2007).
- [14] E. Wimmer *et al.*, *Phys. Rev. B* **24**, 864 (1981); H. J. F. Jansen and A. J. Freeman, *ibid.* **30**, 561 (1984).
- [15] J. P. Perdew, K. Burke, and M. Ernzerhof, *Phys. Rev. Lett.* **77**, 3865 (1996).
- [16] Z. Sun *et al.*, *Phys. Rev. B* **78**, 075101 (2008) have shown that the GGA is superior to LDA+U in the description of these systems, implying that Coulomb correlations do not play a major role in the effects described here. They also find a very weak bilayer-bilayer splitting in the AF phase, which is absent in our work because we assumed AF coupling between bilayers.
- [17] This scheme was used with great success to explain the trends with doping level in $\text{La}_x\text{Ca}_{1-x}\text{MnO}_3$. See W. Luo *et al.*, *Phys. Rev. Lett.* **99**, 036402 (2007).
- [18] M. Kubota *et al.*, *J. Phys. Soc. Jpn.* **69**, 1606 (2000).
- [19] R. Seshadri *et al.*, *Solid State Commun.* **101**, 453 (1997).
- [20] In the FM case, the states of d_{xy} symmetry (minority spin) result in two slightly split cylinders (3 and 3') around Γ [not shown in Fig. 2(b)].
- [21] C. Jozwiak *et al.*, preprint arXiv:0806.2120.
- [22] Bilayer splitting at $x=0.4$ is observable in magnetic Compton profiles [10]. Some differences between bulk probes and photoemission are expected given the latter's surface sensitivity.
- [23] J. Rath and A. J. Freeman, *Phys. Rev. B* **11**, 2109 (1975).
- [24] L. Vasilii-Doloc *et al.*, *Phys. Rev. Lett.* **83**, 4393 (1999); B. J. Campbell *et al.*, *Phys. Rev. B* **65**, 014427 (2001).
- [25] D. S. Dessau and S. Rosenkranz, private communication.
- [26] H. J. Schulz, *Phys. Rev. Lett.* **64**, 1445 (1990).